JGP Journal of General Physiology

ARTICLE

Pore-forming transmembrane domains control ion selectivity and selectivity filter conformation in the KirBac1.1 potassium channel

Marcos Matamoros and Colin G. Nichols

Potassium (K^+) channels are membrane proteins with the remarkable ability to very selectively conduct K^+ ions across the membrane. High-resolution structures have revealed that dehydrated K^+ ions permeate through the narrowest region of the pore, formed by the backbone carbonyls of the signature selectivity filter (SF) sequence TxGYG. However, the existence of nonselective channels with similar SF sequences, as well as effects of mutations in other regions on selectivity, suggest that the SF is not the sole determinant of selectivity. We changed the selectivity of the KirBac1.1 channel by introducing mutations at residue I131 in transmembrane helix 2 (TM2). These mutations increase Na^+ flux in the absence of K^+ and introduce significant proton conductance. Consistent with K^+ channel crystal structures, single-molecule FRET experiments show that the SF is conformationally constrained and stable in high-K^+ conditions but undergoes transitions to dilated low-FRET states in high-Na^+/low-K^+ conditions. Relative to wild-type channels, I131M mutants exhibit marked shifts in the K^+ and Na^+ dependence of SF dynamics to higher K^+ and lower Na^+ concentrations. These results illuminate the role of I131, and potentially other structural elements outside the SF, in controlling ion selectivity, by suggesting that the physical interaction of these elements with the SF contributes to the relative stability of the constrained K^+-induced SF configuration versus nonselective dilated conformations.

Introduction

The exquisite ability to discriminate between K^+ and Na^+, or other monovalent cations, yet at the same time to permeate K^+ ions at close to diffusion-limited rates, allows K channels to play an essential physiological role in controlling electrical properties of the cell membrane and modulating cell function. There is overwhelming evidence that the narrowest part of the pore, formed by the backbone carbonyls of the TxGYG channel signature sequence, generates the K^+ selectivity filter (SF; Doyle et al., 1998; Zhou et al., 2001; Roux, 2017). Hyperpolarization-activated cyclic nucleotide-gated (HCN) channels have a related GYG-containing SF sequence yet allow significant Na^+ permeability. In HCN1 cryo-EM structures, the filter can adopt a nonconanical conformation in which only two of the cation binding sites are formed (Lee and MacKinnon, 2017), as is also seen in NaK, a nonselective channel in which the SF sequence is replaced by TVGDG (Shi et al., 2006). Changes in K channel SF crystal structures with ion concentration (Roux et al., 2011; Roux, 2017; Noskov et al., 2004) and structures that reveal disrupted, presumably inactivated SF conformations (Cuello et al., 2010; Bhate et al., 2010; Cordero-Morales et al., 2007) argue against any simplistic view that the K channel SF must always adopt a rigid canonical structure. Moreover, molecular simulations have consistently indicated that the filter structure should be dynamic (Wang et al., 2016; Wang et al., 2019), with an uneven contribution of the SF K binding sites to selectivity (Noskov et al., 2004). Using single-molecule FRET (smFRET) to assess intramolecular movements in real time (Wang et al., 2016; Wang et al., 2019), we have shown that the predominantly K^+-selective KirBac1.1 channel SF transitions between distinct conformations as a function of the ionic milieu, from a constrained K^+-selective conformation in the presence of K^+ to dilated Na^+-selective conformations in the absence of K^+ (Wang et al., 2019). That study revealed that the constrained conformation is actually induced by the presence of K^+ ions, rather than being preformed and independent of the presence of permeant ions (Wang et al., 2019).

The latter study thus provides experimental evidence that the K channel SF can adopt distinct conformations that depend at least in part on the nature of the permeant ions themselves. The SF is surrounded by other structural elements that do not

Center for Investigation of Membrane Excitability Diseases, and Department of Cell Biology and Physiology, Washington University School of Medicine, St. Louis, MO.

Correspondence to Colin G. Nichols: cnichols@wustl.edu.

contact permeant ions, and multiple studies have shown that K^+ selectivity can be modulated by mutations outside the SF (Yi et al., 2001; Bichet et al., 2004; Bichet et al., 2006) and by the polarizability of surrounding residues (Rossi et al., 2013). In the present study, we use ion flux experiments to examine the functional effect of non-SF mutations in the neighboring transmembrane helix 2 (TM2) on KirBac1.1 ion selectivity and smFRET experiments to examine the effect on SF conformations. The results provide evidence for a simple model in which modulation of ion selectivity by such mutations results from shifting the relative stability of constrained (i.e., K^+-selective) versus dilated (i.e., Na^+-selective) conformations of the SF.

Materials and methods

Plasmids

Plasmids containing tandem dimeric KirBac1.1 protein-encoding cDNAs (T120C-WT and T120C-WT [I131M]) were constructed as described in previous studies using the pQE60 expression vector (Amp^r; Wang et al., 2019; Wang et al., 2016). For KirBac1.1 mutants, mutations were introduced by QuikChange II XL site-directed mutagenesis kit (Agilent) and confirmed by DNA sequencing.

Protein expression and purification and fluorophore labeling

Homotetrameric and tandem dimeric KirBac1.1 (WT and mutant) proteins were expressed and purified following protocols reported previously (Enkvetchakul et al., 2004; Wang et al., 2009; Wang et al., 2019; Wang et al., 2016). The metal affinity-purified proteins were passed through a Superdex-200 10/300 size-exclusion column (GE Healthcare) with running buffer containing 20 mM HEPES, 150 mM KCl, and 5 mM decyl maltoside, pH 7.0. Tetrameric fractions were pooled and concentrated via Amicon Ultra-4 centrifugal filter (MWCO 100 kD; Millipore). Fluorophore labeling was started immediately after gel filtration by adding 1:1 (molar ratio) mix of Alexa Fluor 555 and 647 c2 maleimide to protein solution at final protein:fluorophore molar ratio of 1:5. Labeling reactions proceeded at room temperature for 1 h and were terminated by the addition of 2-mercaptoethanol at a final concentration of 10 mM. A second metal affinity purification was performed to remove free fluorophores or those associated with protein through noncovalent bonds. The labeled proteins were loaded onto a size-exclusion column (Superdex-200 10/300; GE Healthcare), and tetrameric fractions were collected and concentrated for liposome reconstitution. A labeling control using KirBac1.1 WT protein without intrinsic cysteine was always included to evaluate fluorophores bound nonspecifically or associated with protein through noncovalent bonds. All purifications were performed at 4°C except for labeling reactions.

Protein reconstitution

POPE (1-palmitoyl-2-oleoyl-*sn*-glycero-3-phosphoethanolamine) and POPG (1-palmitoyl-2-oleoyl-*sn*-glycero-3-phospho-(1′-*rac*-glycerol)) lipids (3:1, wt/wt) were dissolved in buffer containing 20 mM HEPES, 150 mM KCl, and 30 mM 3-(3-cholamidopropyl) diethylammonio-1 propanesulfonate, pH 7.5, at a final concentration of 10 mg/ml. Protein labeled with Alexa Fluor 555 and 647 fluorophores was mixed with lipid solution at a protein:lipid ratio of 1:200 (wt/wt), with 2% biotinylated-POPE (wt/wt of the total lipids). The lipid/protein mix was incubated at room temperature for 20 min and then passed through a Sephadex G-50 desalting column to remove detergents, thereby forming proteoliposomes. Residual detergents were removed by dialysis against 1 liter of buffer containing 20 mM HEPES and 150 mM KCl or NaCl, pH 7.5, three times, and proteoliposomes were harvested and stored at −80°C for single-molecule imaging.

Single-molecule imaging

Chamber slides were prepared following the protocol of Joo and Ha (2012a). An objective-based TIRF microscope, built on a Nikon inverted microscope (TE-2000s) with 100× APO TIRF NA1.49 objective lens and 532- and 640-nm lasers, was used for single-molecule imaging. Donor and acceptor emissions were separated by OptoSplit II (Cairn) with a 638-nm longpass beam splitter, passed through 585/65- and 700/75-nm emission filters (Chroma), and then collected by an Evolve 512 delta electron-multiplying charge-coupled device camera (Photometrics). A CRISP autofocus system (ASI) was incorporated to compensate for focus drift due to mechanical vibrations and thermal fluctuations. Liposomes containing fluorophore-labeled KirBac1.1 proteins were immobilized on the slide surface by biotin-neutravidin interactions with biotinylated-POPE in liposomes. Fluorophores were excited by a 532-nm laser, and videos were collected using NIS-element (Nikon) with frame rates of 10 frames/s (i.e., time resolution of 100 ms). Laser power was ∼9.1 W/cm^2 (at the objective lens side). Recording times were 2 min, with half bleaching times typically ∼45 s. Except for the 20 mM HEPES and different concentrations of cations, all imaging buffers contained ∼3 mM 6-hydroxy-2,5,7,8-tetramethylchroman-2-carboxylic acid (Trolox), 2 mM 4-nitrobenzyl alcohol, 2 mM cyclooctatetraene, 5 mM protocatechuic acid, and 15 µg/µl protocatechuate-3,4-dioxygenase to enhance the photostability of the fluorophores (Aitken et al., 2008; Dave et al., 2009). 50 µM β-escine was used to permeabilize liposomes (Fan and Palade, 1998; Wang et al., 2019) for experiments with symmetric ionic conditions. Control liposomes reconstituted with labeled control KirBac1.1 WT protein at the same concentration were included to evaluate the fluorescent impurities, ensuring that they were <5% in comparison with sample liposomes. For every protein, at least two independent labeled samples were used; for every sample, ≥10 videos were collected.

Single-molecule imaging data analysis

For every video, individual molecules were identified, and donor and acceptor fluorescence intensity profiles were extracted by IDL scripts developed by the Ha group (Joo and Ha, 2012b; Roy et al., 2008). Leak and direct excitation corrections were not applied, as leakage was <0.06, and direct excitation was undetectable. Traces were inspected and selected manually following criteria described in previous publications (Wang et al., 2018; Wang et al., 2019; Wang et al., 2016). The bin size of all time histograms was set as 0.025 of recording time, ensuring an equal contribution from each trace to avoid dominant effects of long

traces (Blanco and Walter, 2010). FRET contour plots were generated from the first 3 s of each trace. For idealizing smFRET traces using HaMMy software (McKinney et al., 2006), FRET traces in the same condition used to make the histograms were concatenated into a single file. Subsequent transition analysis was performed using TDP (McKinney et al., 2006), Microsoft Excel, and GraphPad Prism 6.

Fluorescence liposome flux assay

KirBac1.1 proteins were reconstituted into POPE/POPG liposomes with a protein:lipid ratio of 1:500, by passing through Sephadex G-50 desalting columns equilibrated with buffer (20 mM HEPES and 150 mM KCl or NaCl, pH 7.5). Immediately before flux assay, the extraliposomal buffer was replaced by buffer containing 150 mM NMDG. 9-Amino-6-chloro-2-methoxyacridine (ACMA) stock was then added to reach a final concentration of 13 µM into a 96-well plate. Baseline fluorescence (excitation wavelength 400/30 nm and emission wavelength 495/10 nm; Top50 Mirror) was measured by a Synergy 2 plate reader as previously described (Wang et al., 2019). All flux data were normalized to the maximum quenching after valinomycin or monensin addition, and the values of empty liposomes were subtracted in each condition.

Radioactive rubidium and sodium flux assays

KirBac1.1 proteins were reconstituted, and $^{86}Rb^+$ and $^{22}Na^+$ flux assays were performed as described previously (Wang et al., 2019).

Statistics

The FRET histogram data for each sample/condition were presented as equal contributions from all individual molecule traces (rather than each data point). The FRET contour map for each sample/condition was calculated from the first 3 s of all traces, with equal contributions from all individual traces (all selected traces were >5 s). The trace number *n* for each sample/condition is included in the accompanying figure legends as published previously (Wang et al., 2018; Wang et al., 2019; Wang et al., 2016). For each condition, FRET data were split into three different datasets with a similar number of traces coming from multiple different videos in each case, to assess variability. The number of videos for each of the three subsets (i, ii, and iii) are as follows: for WT from 150 mM NaCl to 150 mM KCl sequence as in Fig. 10: 150 mM NaCl, 6, 6, 9; 150 mM NaCl/0.5 mM KCl, 5, 2, 4; 150 mM NaCl/5 mM KCl, 15, 16, 14; 100 mM NaCl/50 mM KCl, 4, 11, 6; 5 mM NaCl/150 mM KCl, 2, 10, 5; 0.5 mM NaCl/150 mM KCl, 6, 3, 8; 0.05 mM NaCl/150 mM KCl, 3, 5, 8; and 150 mM KCl, 15, 5, 10; and for I131M, 13, 8, 12; 2, 4, 7; 13, 12, 16; 4, 5, 5; 3, 4, 6; 3, 6, 8; 4, 8, 10; and 6, 10, 7, respectively. The calculated rate constants and state probabilities are therefore represented as mean ± SEM of $n = 3$ datasets. To assess state dwell time distributions in Fig. 9, full datasets without splitting were used to fit monoexponential decay functions. Time constants are represented as mean ± 95% confidence interval of the fitting. All flux data are presented as mean ± SEM.

Code availability

The script used to convert TIF video files to PMA files for later data processing is available upon request. IDL scripts developed by the Ha group (fully described in Joo and Ha [2012b] and Roy et al. [2008]) were used for video data processing (PMA files). Subsequent analysis was performed using Microsoft Excel and GraphPad Prism 6.

Data availability

All data generated or analyzed during this study are included in this article or are available from the corresponding authors upon reasonable request.

Online supplemental material

Fig. S1 shows K-driven $^{86}Rb^+$ efflux at different pH values. Fig. S2 shows the functionality of tandem dimers, after labeling. Fig. S3 shows concatenated smFRET trajectories in high-Na/low-K conditions. Fig. S4 shows concatenated smFRET trajectories in high-K/low-Na conditions. Table S1 lists the number of individual molecules and identified transitions for idealized smFRET records. Table S2 lists rate constants for the three-state model.

Results

Previous studies have demonstrated that mutation of certain residues in the TM2, outside the SF, can significantly alter the selectivity of at least two K channels, e.g., Kir3.2 (S177W/G; Bichet et al., 2006; Bichet et al., 2004; Yi et al., 2001) and K channel of *Streptomyces lividans* (KcsA; M96V; Renart et al., 2012). Mechanistic explanation for these findings has been absent, but our recent results (Wang et al., 2019) raise the possibility that the steric interaction of these mutations with the SF might alter the relative stability of constrained versus dilated conformations. To examine this, we introduced mutations in KirBac1.1 at the equivalent I131 position (Fig. 1, A and B), purified recombinant tetrameric proteins, and assessed reconstituted channel activity and structural dynamics in liposomes.

Mutations in TM2 reduce K selectivity

The favored binding of K^+ (or Rb^+) over Na^+ in the K channel SF is required for conduction of K^+ at high rates and selection over other ions. As we have shown in KirBac1.1 WT, the constrained K^+-selective conformation is dependent on the presence of K^+ ions themselves, while dilated, dynamic, SF conformations in pure Na^+ solutions are correlated with Na^+ permeating states. We directly tested selective permeation of KirBac1.1 I131x mutants by examining radioactive ion uptake into KirBac1.1-containing liposomes, under driving forces generated solely by K^+ or Na^+ ions (Fig. 1, C and D), as previously described for KirBac1.1 or KcsA (Cheng et al., 2011; Enkvetchakul et al., 2004; Wang et al., 2019). While K^+- and Na^+-driven $^{86}Rb^+$ fluxes are similar for WT and mutant subunits (except for the I131G mutant, which is lower; Fig. 1 E), Na^+-driven $^{22}Na^+$ fluxes are clearly higher in KirBac1.1 I131M than in WT, implying increased Na^+ ion permeation and a relative decrease in selectivity (Fig. 1 F). Importantly, we also detected $^{22}Na^+$ fluxes when the driving force was generated by K^+ ions, but these were much smaller than Na^+-driven fluxes (Fig. 1 F, right), suggesting that Na^+ permeation through KirBac1.1 WT and I131x is actually inhibited by K^+, consistent with previous findings that the ion configuration

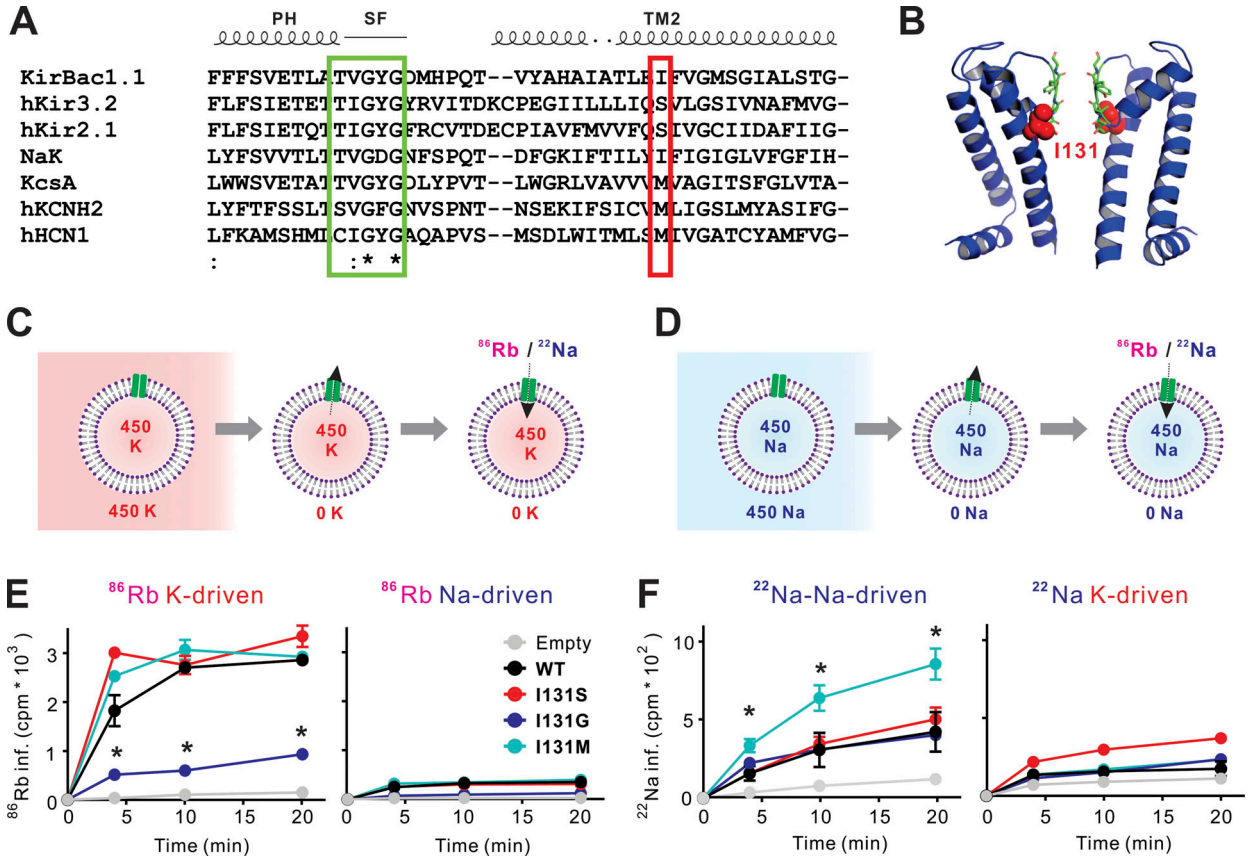

Figure 1. **Changes in permeant ion-induced conductance between KirBac1.1 WT and I131x mutants. (A)** Sequence alignment of SF signature sequences and TM2 of potassium channels. SF in green and I131 equivalent position in red. **(B)** Crystal structure of KirBac1.1 SF and transmembrane domains with residues forming K binding sites highlighted in green and I131 position in red. **(C and D)** Cartoon diagram of K-driven $^{86}Rb^+$ or $^{22}Na^+$ assays (C) or Na-driven assays (D). **(E)** Time course of $^{86}Rb^+$ uptake into liposomes (POPE:POPG, 75:25%), with 450 mM internal K^+ (left) or Na^+ (right). Inf, influx. **(F)** Time course of $^{22}Na^+$ uptake into liposomes (POPE:POPG, 75:25%), with 450 mM internal K^+ (left) or Na^+ (right). Liposomes were reconstituted with no protein (empty, gray), KirBac1.1 WT (black), or KirBac1.1 I131S/G/M (red, blue, and green, respectively; 2 µg/mg lipid). *, $P < 0.05$ versus. WT. All data are represented as mean ± SEM of at least $n = 3$ experiments.

within the SF is an important determinant of selectivity in K channels (Cheng et al., 2011; Thompson et al., 2009; Valiyaveetil et al., 2006; Wang et al., 2019).

I131x mutants increase Na^+ flux and generate proton permeation

To further assess ion selectivity, purified WT or mutant KirBac1.1 channels were reconstituted into liposomes in the presence of 150 mM KCl or NaCl (Fig. 2 A). Vesicles were then diluted into an (impermeant) ACMA-NMDG–containing solution (low K/Na phase), which creates a strong chemical gradient for the efflux of K^+ or Na^+. In the assay, K^+ or Na^+ efflux is then initiated by the addition of the H^+ ionophore carbonyl cyanide *m*-chlorophenylhydrazone (CCCP), which allows influx of H^+ to counter the efflux of K^+ or Na^+ (CCCP phase). H^+ influx is monitored by H^+-dependent quenching of ACMA fluorescence. Finally, a K^+ or Na^+ ionophore (valinomycin or monensin, respectively) is added to allow complete dissipation of the gradient (Fig. 2, A and B).

Each of the KirBac1.1 I131 mutants were expressed at levels similar to WT, and each showed similar overall K^+ fluxes, but all showed significantly higher fluxes of sodium in the absence of K^+ (Fig. 2 B), consistent with a loss of K^+ selectivity. Surprisingly, the fluorescent assay additionally indicates that these mutations also introduce significant proton permeation (Fig. 2, B and C). As shown in Fig. 2, B and C, the fluorescent signal is stable after adding empty liposomes or liposomes containing WT channels (low-XCl phase), until CCCP is added to initiate proton flux, indicating essentially no proton permeability of the liposomes themselves, or the WT channel. However, after adding liposomes containing any of the mutant channels, in particular I131G, there is a rapid and significant decay in fluorescent signal, even before adding CCCP, indicating intrinsic proton permeability of these mutants (Fig. 2, B and C). In addition, while the I131G mutant has markedly lower $^{86}Rb^+$ uptake than WT under control conditions (pH 7 inside and outside; Fig. 1 E), uptake is also much more pH sensitive than WT: increasing external pH from 7 to 9 increases $^{86}Rb^+$ uptake fourfold in the mutant, but only twofold in WT (Fig. S1). This suggests that the proton gradient can help to drive $^{86}Rb^+$ permeation in I131G and that the intrinsic ion permeability of this mutant is actually high, as indicated by the ACMA assays (Fig. 2 B). Proton "wires,"

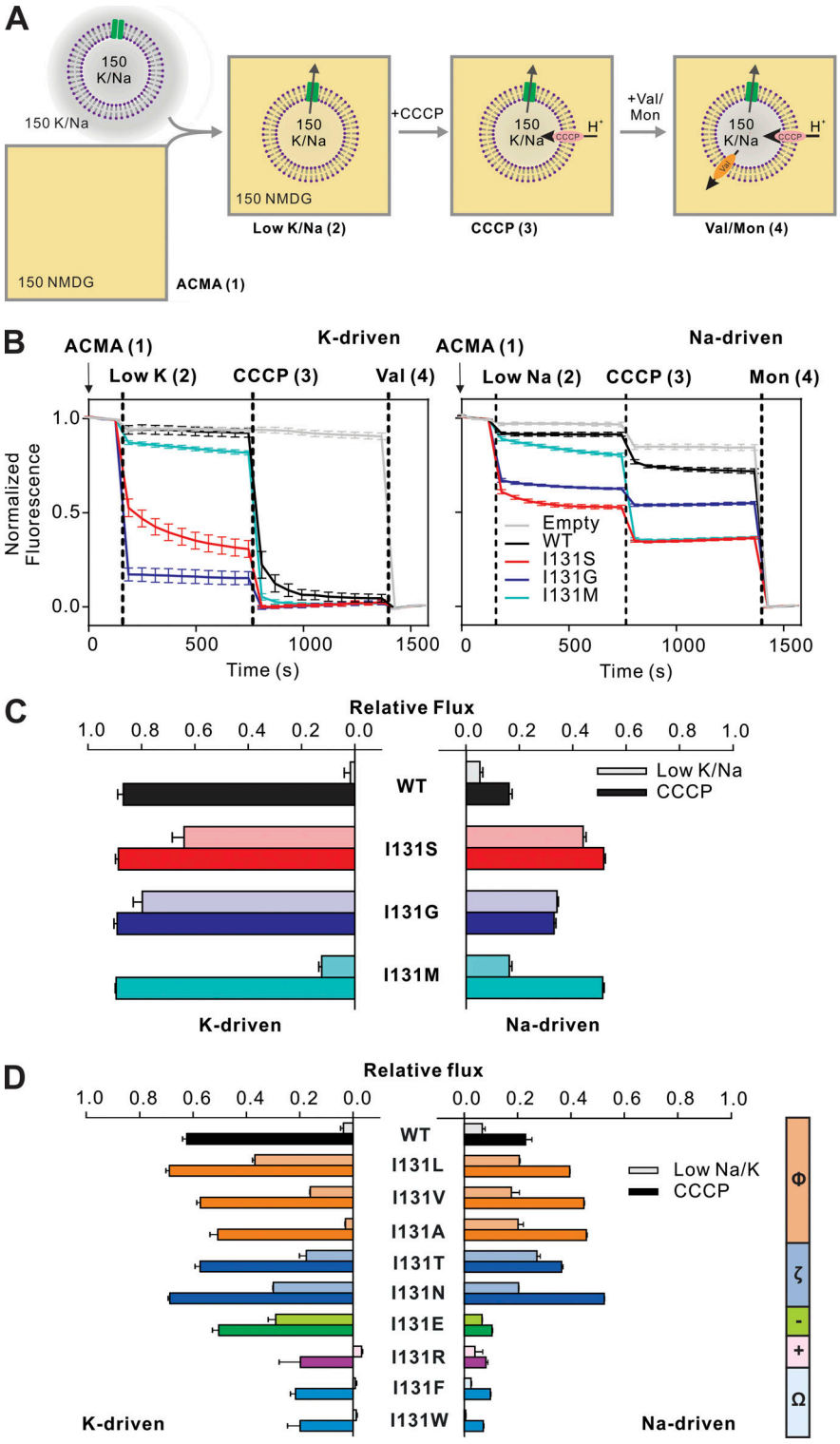

Figure 2. **Mutations at position I131 alter KirBac1.1 ion selectivity and generate proton translocation. (A)** Cartoon diagram of ACMA fluorescence-based assays with KirBac1.1 channels embedded in liposomes. (1) ACMA/150 mM NMDG solution. Maximal ACMA fluorescence is present due to no liposome addition. (2) Liposomes that are generated with high (150 mM) Na^+ or K^+ on both sides are diluted in the ACMA/150 mM NMDG solution. Solution is switched to low (nominally zero) Na^+ or K^+. ACMA fluorescence is maintained, unless counterion flow allows Na^+ or K^+ efflux. (3) Addition of CCCP allows counterion entry of protons to quench ACMA fluorescence, in proportion to Na^+ or K^+ efflux. (4) Monensin or Valinomycin addition allows maximal Na^+ or K^+ efflux, respectively. **(B)** K^+-driven (left) and Na^+-driven (right) fluxes. WT KirBac1.1 K^+ and Na^+ fluxes (black line) are minimal unless CCCP is added. I131S/G/M (red, blue, and green lines, respectively) mutants translocate protons in absence of CCCP and increase channel-dependent Na^+ fluxes. **(C)** Relative flux calculated from B at the end of the low-Na/K phase (2; light color) and at the end of CCCP phase (3; dark), normalized to maximum ACMA fluorescence in high [K^+/Na^+] (1) and minimum fluorescence in Val/Mon (4) after subtraction of empty liposome values. **(D)** Relative flux calculated as in C, for additional I131 mutants, as indicated. Amino acids are grouped as hydrophobic (orange, Φ), hydrophilic (blue, ζ), negatively charged (green, –), positively charged (purple, +), and aromatic (light blue, Ω). All data are represented as mean ± SEM of at least n = 3 experiments.

hydrogen-bonded chains allowing protons to tunnel through the membrane, have been identified in multiple membrane proteins, including serotonin transporters (Cao et al., 1997), in bacteriorhodopsin (Wikström, 1998; Bondar et al., 2008) or cytochrome c oxidase (Hofacker and Schulten, 1998; Namslauer et al., 2007), and after replacing S4 arginines by histidine in the *Shaker* potassium channel, which creates a proton permeation path through the voltage sensor domain (Starace and Bezanilla, 2004; Starace and Bezanilla, 2001; Starace et al., 1997). The proton path in these I131 mutants is unclear at this juncture.

To assess the relevance of specific structure, functional K channels were reconstituted from multiple amino acid 131 substitutions. Both sodium and proton permeability was present in hydrophilic or negatively charged, and even relatively large hydrophobic, amino acid mutants (I131G/M/S/T/E/A/N/L), but

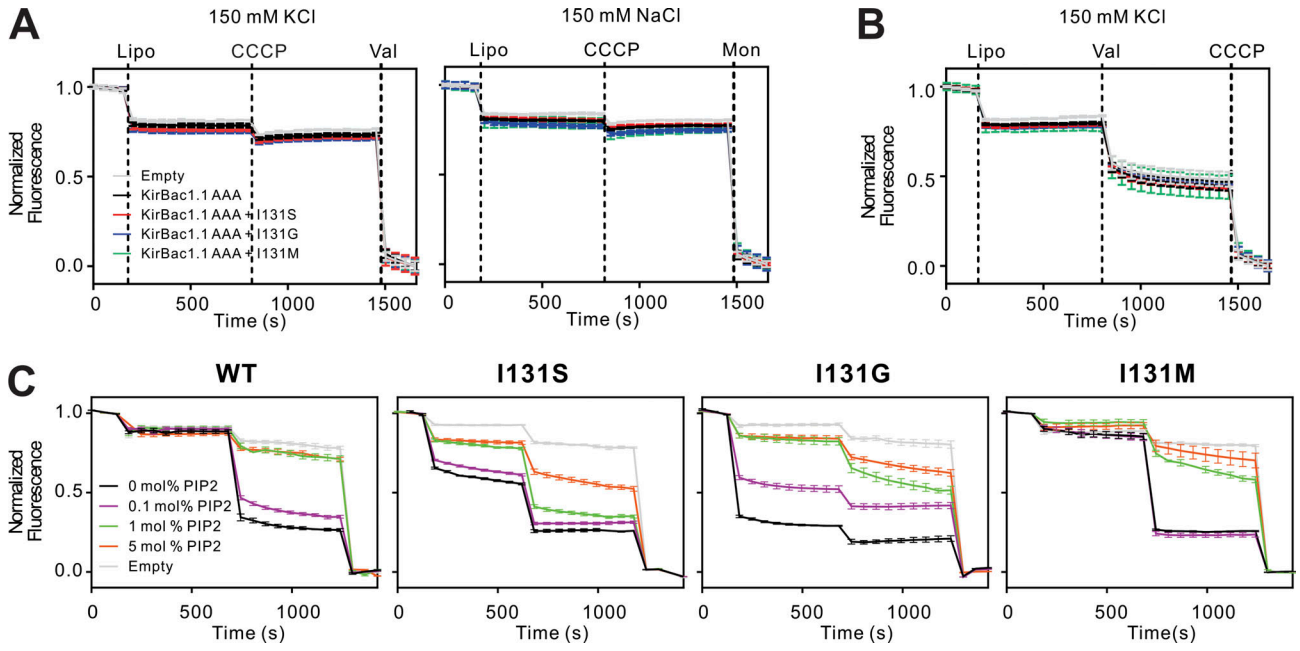

Figure 3. **Proton permeation is blocked by AAA mutation and by PIP_2 addition. (A and B)** The AAA SF mutation (in which the SF GYG sequence is replaced by AAA) was introduced on the I131x mutation backgrounds. All mutants show no activity in either K^+ or Na^+ conditions (A) and no H^+ permeation above that for empty liposomes (Lipo) when valinomycin (Val) is added instead of CCCP (B). **(C)** Fluorescence assays for WT and I131S/G/M mutants in K^+ conditions as a function of membrane [PtdIns(4,5)P_2]. All data are represented as mean ± SEM of at least n = 3 experiments.

was not apparent in positively charged and aromatic substitution mutants (I131F/W/R; Fig. 2, C and D), which also exhibited lower overall fluxes. We found that both ion and proton flux through I131x mutants were abolished by replacement of the SF GYG sequence with AAA. None of the mutants showed activity in K^+ or Na^+ conditions (Fig. 3 A), and valinomycin-induced proton flux in the absence of CCCP is not different from that for empty liposomes (Fig. 3 B).

Finally, in contrast to all eukaryotic Kir channels, KirBac1.1 channel activity is inhibited by phosphatidylinositol phosphates, such as phosphatidylinositol 4,5-bisphosphate (PIP_2; Enkvetchakul et al., 2004; Cheng et al., 2009). Both ion and proton permeation through I131x mutants are inhibited by PIP_2 at different concentrations (Fig. 3 C). While not providing a definitive test, these results are consistent with a common pathway for both protons and permeant ions.

E106-D115 hydrogen bond disruption does not alter K selectivity in KirBac1.1

In some K channels, a glutamate–aspartic acid hydrogen bond or glutamate-arginine salt bridge behind the SF is involved in maintaining the SF structure. Disruption of the E71–D80 hydrogen bond in KcsA or the E138–R148 salt bridge in Kir2.1 or Kir3.1 reduces K selectivity (Cheng et al., 2011; Yang et al., 1997; Dibb et al., 2003). Specifically, the KcsA [E71A] and Kir2.1 [R138E, E148R] mutants exhibit reduced selectivity for K^+ over Na^+ compared with WT in the absence of K^+, in which conditions WT channels become nonconductive. Although this bridge is not conserved throughout K channels, KirBac1.1 has a glutamate/aspartate residue pair (E106–D115) that could form a hydrogen bond equivalent to that in KcsA (Fig. 4, A and B). However, multiple single or double substitutions of E106 or D115 result in functional channels that maintain K selectivity and do not show proton permeation (Fig. 4 C). These data suggest that the E106–D115 residues are not involved in maintaining the K selectivity in KirBac1.1 channels.

Mutations in TM1 can restore K selectivity

Previously, introduction of a secondary mutation (Y102N) in transmembrane domain 1 (TM1) on the nonselective Kir3.2 [S177W] background (Kir3.2 [Y102N,S177W]) was shown to recover K^+ selectivity (Bichet et al., 2004). It has been hypothesized that in the KirBac1.1 equivalent position F71, the aromatic side chain is oriented toward the cavity and can stabilize the open conformation (Fig. 5 A; Amani et al., 2020). Introduction of the equivalent F71N mutation on I131x mutant backgrounds had no effect on ion selectivity, with the notable exception of the F71N, I131G double mutation, which does restore significant K^+/Na^+ selectivity, but without abolishing the proton flux (Fig. 5 B).

I131M mutation shifts the K^+ dependence of smFRET-reported SF conformation

We have developed a smFRET approach that allows real-time assessment of conformational dynamics in functional, liposome-embedded K channels (Fig. 6 A, left; Wang et al., 2019; Wang et al., 2016). With fluorophores placed at diagonal T120C sites of homotetrameric channels (Fig. 6 A), this has revealed K^+ ion–dependent flexibility of the KirBac1.1 SF in functional constructs (Wang et al., 2019; Wang et al., 2016). The same construct with the additional I131M mutation retains K^+ and Na^+ conductance when labeled (Fig. S2). In the present study, we first confirmed that, in the absence of K^+ (replaced with 150 mM Na^+), WT SF signals are dynamic, with low (~0.2) and medium (~0.45) FRET

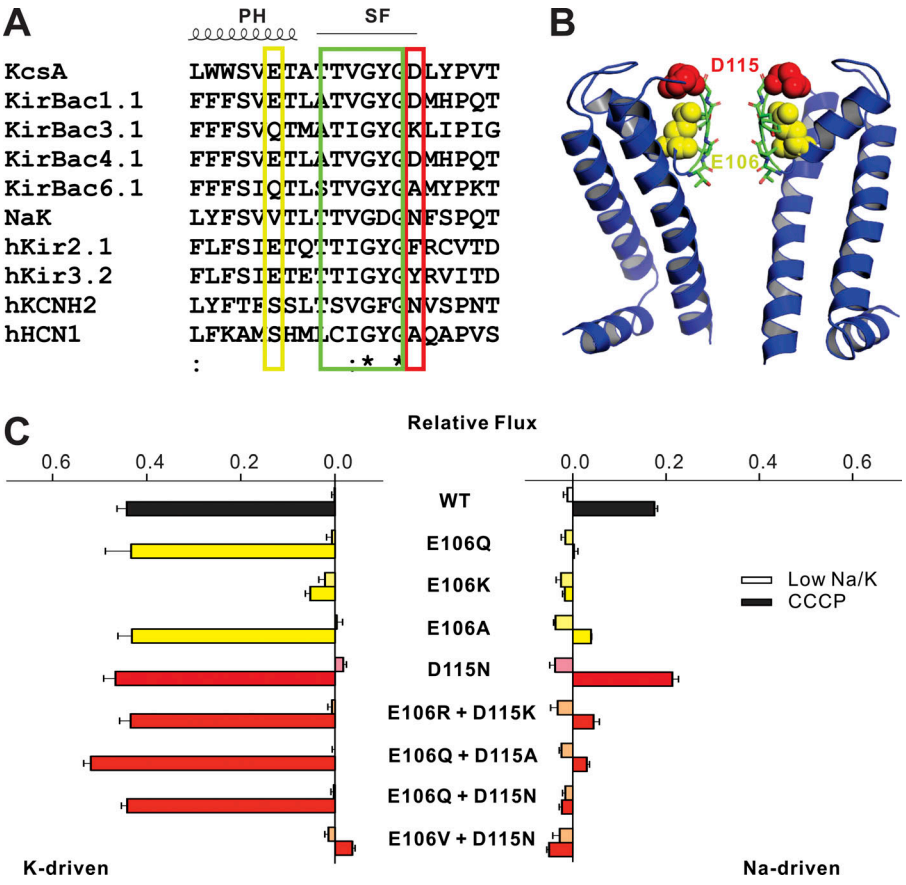

Figure 4. **The E106/D115 residue pair, equivalent to E71/D80 in KcsA, is not involved in maintenance of K selectivity. (A)** Potassium channel SF signature sequence alignments (green) with E106 and D115 equivalent positions in yellow and red, respectively. **(B)** Crystal structure of KirBac1.1 SF and the hydrogen bond behind SF (E106 in yellow and D115 in red), equivalent to E71–D80 in KcsA. **(C)** Relative flux calculated as in Fig. 2, for mutants, as indicated. KirBac1.1 hydrogen bond mutants are functional in 150 mM KCl (left) and maintain K selectivity in 150 mM NaCl (right). All data are represented as mean ± SEM of at least n = 3 experiments.

efficiencies predominating, and then switch to a constrained predominantly high (~0.8) FRET state in the presence of high (150 mM) K^+ (Figs. 6 and 7; Wang et al., 2019). At all $[K^+]$ between 0 and 150 mM, FRET amplitude distributions show clear peaks, requiring a minimum sum of three Gaussians for adequate fitting (Figs. 6 and 7), with the same FRET amplitude peaks at ~0.2, ~0.45, and ~0.8. Addition of K^+ in the presence of 150 mM Na^+ results in a concentration-dependent switch from being primarily dilated (low FRET) and dynamic to being constrained (high FRET), and this is essentially saturated at ~5 mM K^+ for WT KirBac1.1 (Figs. 6 B and 7 B; Wang et al., 2019).

We observe qualitatively similar behavior in I131M channels, but the $[K^+]$ dependence of the FRET distributions is markedly different between WT and I131M channels (Figs. 6 B and 7 B). Dynamic, predominantly low (~0.2) FRET states in 150 mM Na^+ are not obviously suppressed by substitution of up to 50 mM K^+ (Fig. 6 B, bottom); if anything, the low FRET state occupancy is slightly increased. Conversely, addition of only 5 mM Na^+ is sufficient to substantially increase low FRET signals in 150 mM K^+ (Fig. 7, A and B). As shown in Fig. 8, overall FRET sensitivity to $[K^+]$ is reduced ~100-fold in the KirBac1.1 I131M mutant relative to WT (Fig. 8 A), while sensitivity to $[Na^+]$ is increased ~3-

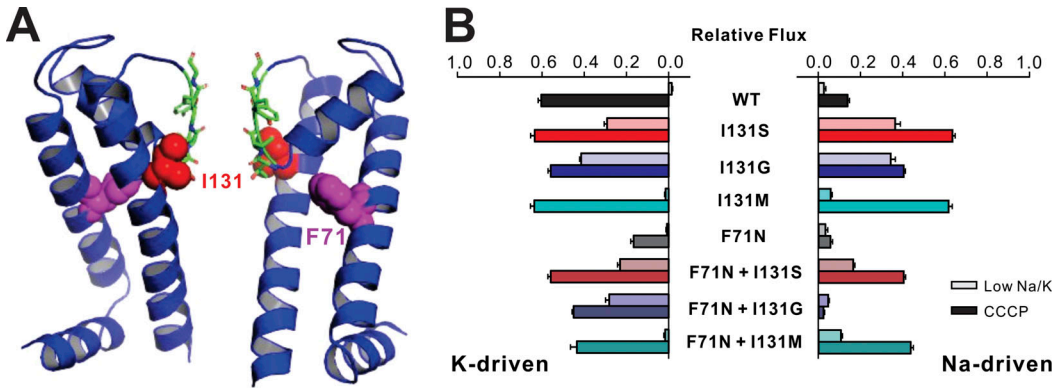

Figure 5. **F71N mutation recovers K selectivity. (A)** Crystal structure of KirBac1.1 SF and transmembrane domains with residues forming K binding sites highlighted in green, I131 position in red, and F71 position in magenta. **(B)** Relative flux calculated as in Fig. 2, for mutants, as indicated. All data are represented as mean ± SEM of at least n = 3 experiments.

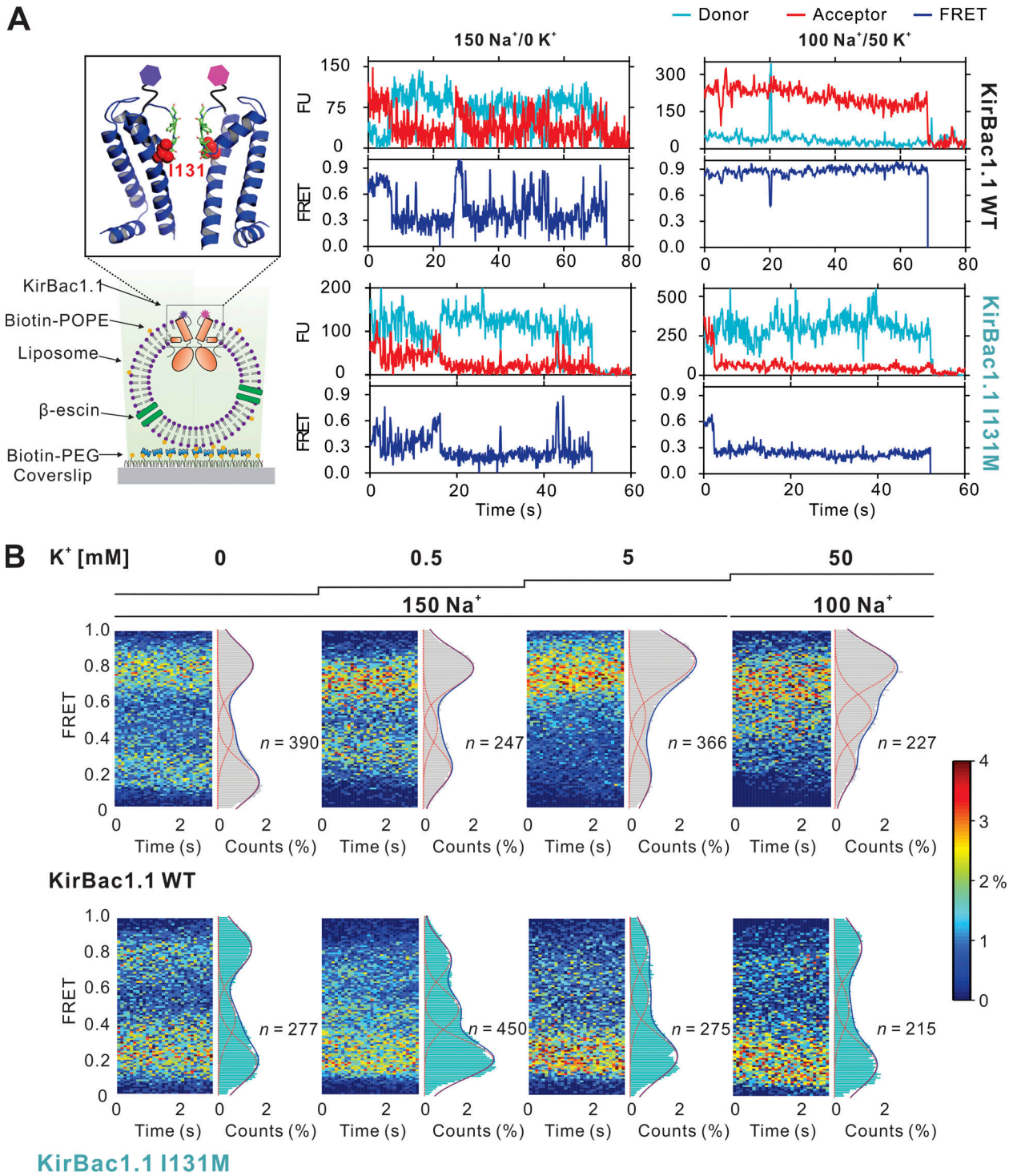

Figure 6. **Mutations in position I131 reduces K sensitivity of KirBac1.1 SF dynamics. (A)** Left: smFRET imaging of KirBac1.1 proteins in liposomes labeled with Alexa Fluor 555/647 c2 maleimide pair. Proteoliposomes were immobilized on a polyethylene glycol (PEG)-coated coverslip surface with biotin-POPE and then permeabilized by 50 µM β-escin to achieve symmetrical ionic conditions. Side view of KirBac1.1 crystal structure indicating diagonally opposed T120C labeling sites (purple and magenta) in the SF loop and I131 position in red. Tetrameric channels are formed from pairs of tandem dimers in which only one protomer contains the cysteine mutation. Due to the asymmetric structures, the two dimers can only assemble anti-parallel, with two cysteine residues at diagonal subunits. Right: Representative smFRET trajectories in different [ion] for KirBac1.1 WT and I131M mutant. Fluorescence intensities of the donor Alexa Fluor 555 and acceptor Alexa Fluor 647 (AF555/647) are colored cyan and red, respectively; calculated FRET is colored blue. FU, fluorescence uptake. **(B)** FRET histograms for AF555/647 fluorophores labeled at diagonal T120C sites in the SF loop in the WT and I131M protein, at increasing [K^+] from 0 to 50 mM on a background of 150 mM Na^+, as indicated (*n* indicates number of traces in each case). In all histograms, over the whole range of [K^+] and [Na^+], the FRET amplitude distributions show clear peaks, requiring a minimum sum of three Gaussians for adequate fitting, with FRET peaks at ∼0.2, ∼0.45, and ∼0.8.

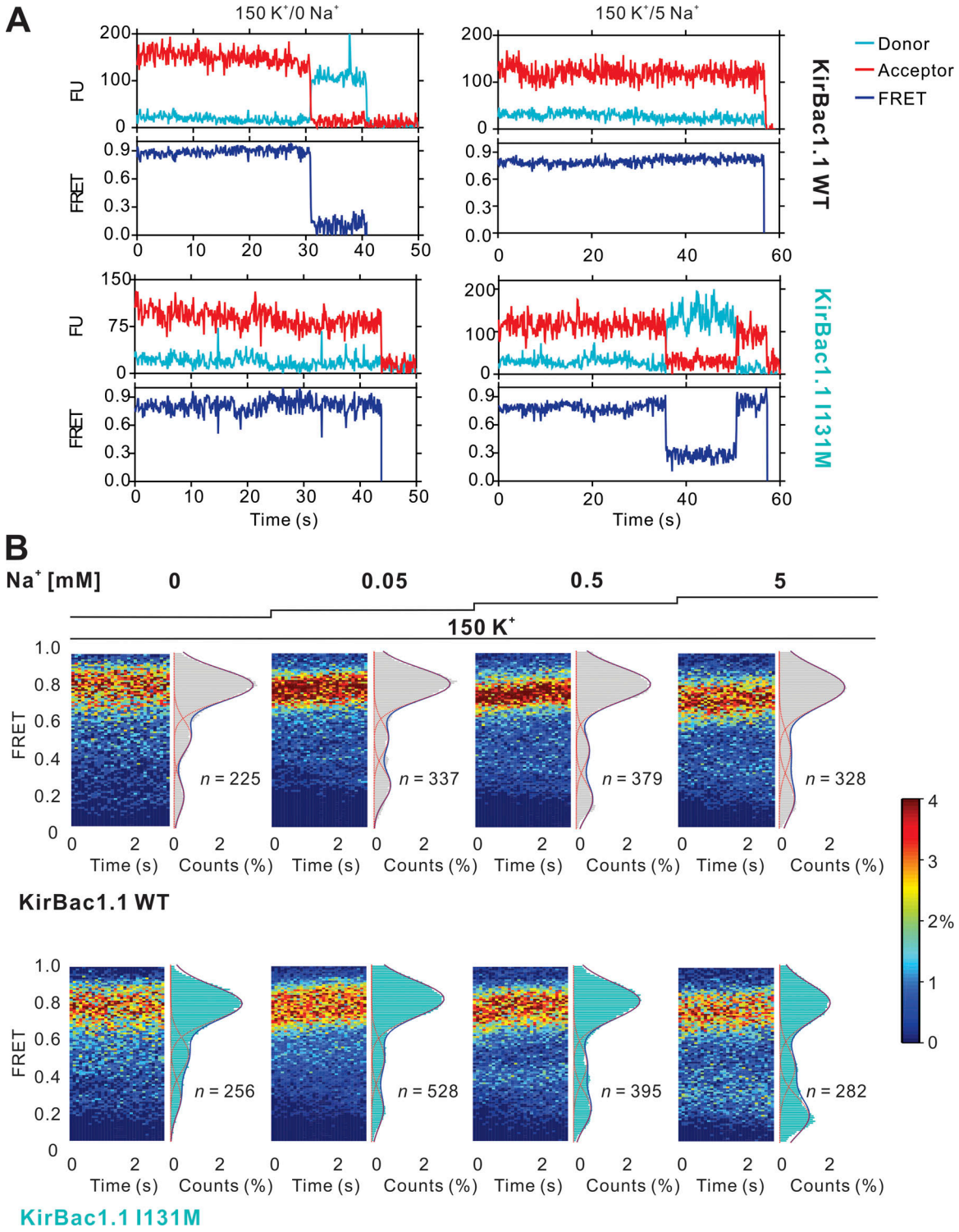

Figure 7. **Mutations at position I131 alter KirBac1.1 SF dynamics at low [Na]. (A)** Representative smFRET trajectories in different [ion] for KirBac1.1 WT and I131M mutant. Fluorescence intensities of the donor Alexa Fluor 555 and acceptor Alexa Fluor 647 (AF555/647) are colored cyan and red, respectively; FRET is colored blue. FU, fluorescence uptake. **(B)** FRET histograms for AF555/647 fluorophores labeled at diagonal T120C sites in the SF loop in the WT and I131M protein, at increasing [Na^+] from 0 to 5 mM on a background of 150 mM K^+, as indicated (*n* indicates number of traces in each case); fits as in Fig. 6.

fold in the mutant (Fig. 8 B). This is consistent with the I131M mutation reducing the intrinsic stability of the constrained, K^+-selective high FRET state, thereby requiring higher [K^+] to achieve the same fractional occupancy.

[K^+]-dependent conformational kinetics

With the caveat that changes in the FRET signal may arise because of changes in anisotropy, rather than separation of the fluorophores, the [K^+] dependence of FRET amplitude distributions

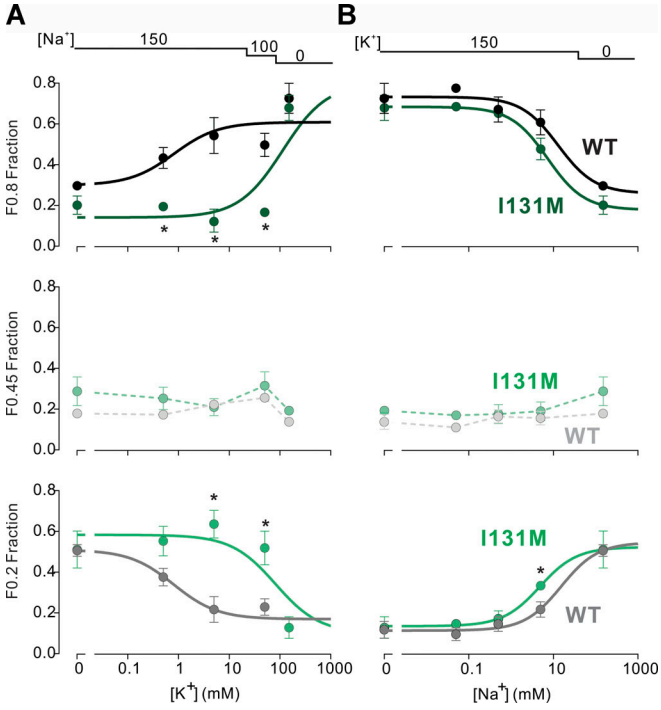

Figure 8. **SF-loop conformation dependence on ion occupancies is shifted in KirBac1.1 I131M. (A and B)** Fractional amplitudes from three-state fits to FRET histograms in Figs. 6 B and 7 B, with sigmoidal equation fits of [ion] dependence of fractional occupancy of high (F0.8) and low (F0.2) states for KirBac1.1 WT (gray) and KirBac1.1 I131M (green), for increasing $[K^+]$ concentrations on a high $[Na^+]$ background (A; F0.8: $K_{1/2}$ WT, 0.81 mM; $K_{1/2}$ I131M, 113.2 mM; F0.45 and F0.2: $K_{1/2}$ WT, 0.8 mM; $K_{1/2}$ I131M, 81.5 mM), and increasing $[Na^+]$ concentrations on a high $[K^+]$ background (B; F0.8: $K_{1/2}$ WT, 12.96 mM; $K_{1/2}$ I131M, 7.29 mM), medium (F0.45), and low (F0.2: $K_{1/2}$ WT, 15.35 mM; $K_{1/2}$ I131M, 4.76 mM). For this figure and Fig. 10, all datasets were split into three equal-sized groups and analyzed separately, to assess variability in the data, which are presented as mean ± SEM of the three data groups. *, $P < 0.05$ versus WT. All data are represented as mean ± SEM.

(Figs. 6 and 7) suggests a simple scenario in which the SF-loop of the two diagonally apposed subunits contributing to the FRET signal are predominantly "dilated," i.e., the fluorophores are relatively away from the pore axis (generating the low FRET 0.2 state, L), in intermediate position (generating the intermediate FRET 0.45 state, M), or constricted toward the pore axis (generating the high FRET 0.8 state, H). We analyzed the kinetics of idealized concatenated FRET records (Fig. 9 A; full dataset in Figs. S3 and S4; see Materials and methods; Wang et al., 2019). To overcome the limitations of short recordings and attempt to estimate lifetimes, we randomly concatenated all trajectories obtained under the same condition (Blanco and Walter, 2010) into three equal records (Fig. 9 A; see Materials and methods; Wang et al., 2019). The total number of molecules (*n*) and the total number of identified transitions (*nt*) are given for each condition in Table S1). As shown in Fig. 9 B, the idealized state lifetimes are distributed approximately exponentially. Single exponential fits to these lifetimes reveal a qualitative dependence on ionic conditions, with H state lifetimes increasing, and L state lifetimes decreasing, as Na^+ is replaced by K^+ (Fig. 9 C). For I131M, this analysis suggests a similar relationship for both, but both appear less sensitive to $[K^+]$ (Fig. 9 C).

The full datasets were also analyzed in terms of a three-state model (Fig. 10 A), assuming free access between states (McKinney et al., 2006). As shown in Fig. 10 B, transition density plots indicate that the most frequent paths are H⇔M, M⇔L, with H⇔L being much less frequent, under all conditions. This analysis indicates the dependence of fractional state occupancy (H, M, and L state probability calculated from the idealization) on ionic conditions: H state occupancy increases, and L state occupancy decreases, as Na^+ is replaced by K^+ (Fig. 10 C). Again, for I131M, this analysis suggests a similar relationship for both, but again both appear less sensitive to $[K^+]$. Not only lifetimes, but also transition paths, are obtained from such idealizations, allowing calculation of individual rate constants for each transition (full dataset in Table S2), which indicate that increase in the M>H (k_{MH}), L>M (k_{LM}), and L>H (k_{LH}) transition rates are the predominant drivers of altered FRET distributions as $[K^+]/[Na^+]$ increases, while the H>M (k_{HM}), M>L (k_{ML}), and H>L (k_{HL}) rates tend to decline as $[K^+]/[Na^+]$ increases. These distributions are similar to those reported from previous WT analysis and generally consistent with an allosteric three-state kinetic model, in which transition rate constants k_{LM}, k_{LH}, and k_{MH} increase, and k_{HM}, k_{HL}, and k_{ML} decrease, as $[K^+]/[Na^+]$ increases (Wang et al., 2019). It is important to note that this analysis pushes the limits of the method but, again, for I131M, there is a trend toward reduced sensitivity of the rate constants to $[K^+]/[Na^+]$, particularly for k_{LM}, k_{MH}, and k_{LH} (Fig. 10 D).

Discussion

Structural basis of K selectivity

All highly K^+-selective members of the cation channel superfamily contain the canonical Gly-Tyr-Gly sequence that generates multiple K^+ ion binding sites in the SF. Intense study, using crystallographic, electrophysiological, and biochemical approaches, has shown that this is unequivocally where K^+ ions are selected over Na^+ ions (Alam and Jiang, 2011; Doyle et al., 1998; Heginbotham et al., 1994; Liu and Lockless, 2013; Lockless et al., 2007; Noskov and Roux, 2006; Roux, 2005; Roux, 2017; Sauer et al., 2011). Despite this unquestioned reality, several findings are not easily accommodated in this framework. In multiple K channels, selectivity can be altered by mutations located outside the SF, including Kir2.1 (Thompson and Begenisich, 2001), Kir3.2 (Bichet et al., 2006; Bichet et al., 2004; Yi et al., 2001), and KcsA (Renart et al., 2012; Cheng et al., 2011). There are channels with similar SF structure that are nonselective, and the simplistic view that the SF is a relatively fixed structure with the appropriate dimensions to accommodate K^+ ions, but not Na^+ ions, has repeatedly been cautioned against (Roux et al., 2011; Roux, 2017; Nimigean and Allen, 2011; Dixit and Asthagiri, 2011; Alam and Jiang, 2011; Andersen, 2011). Our smFRET studies reveal that the SF conformation is actually conformationally dynamic and dependent on the nature of the ions present: rather than being "designed" to accommodate K^+ ions, the canonical K-permeating conformation is actually generated in the presence of K^+ ions, i.e., the

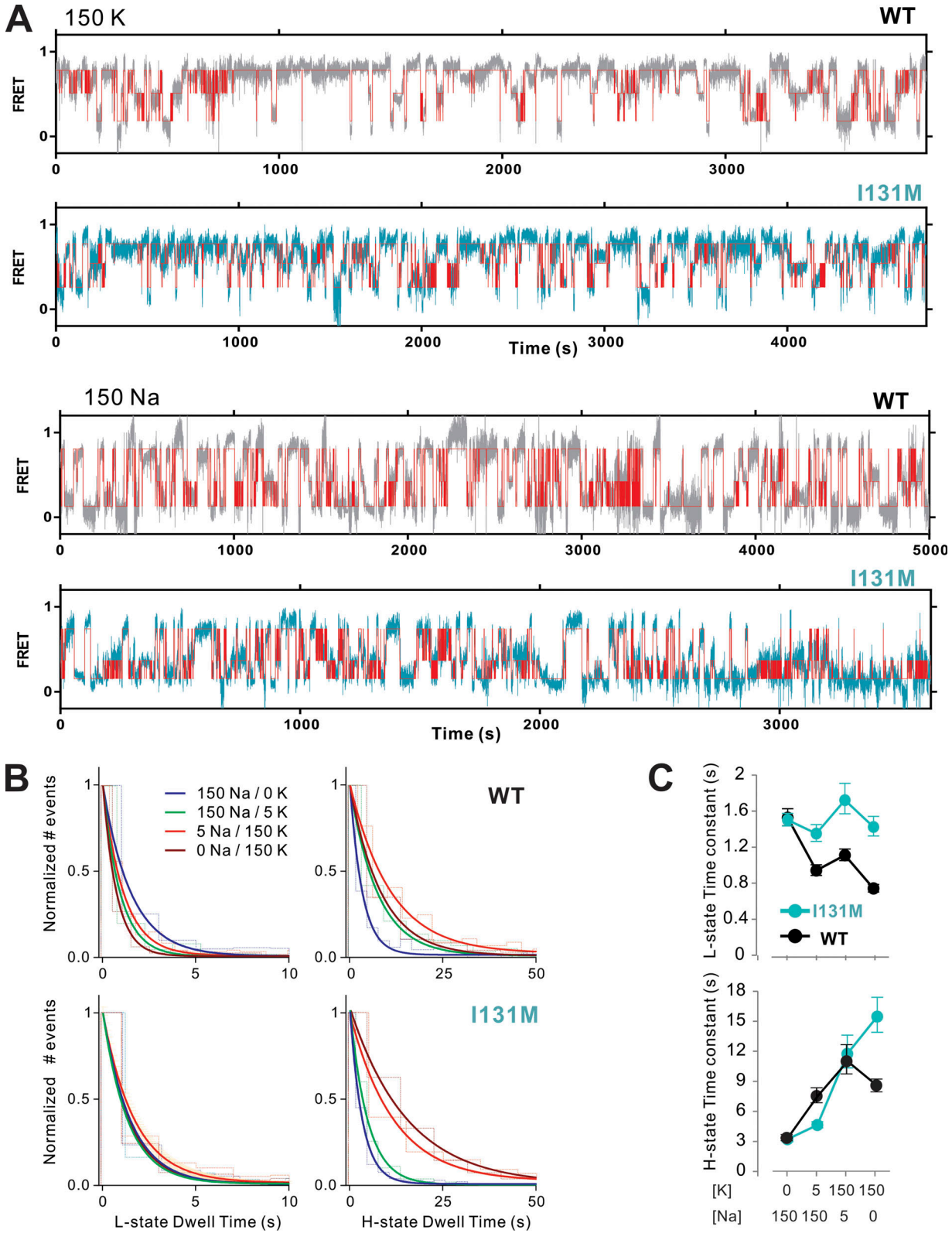

Figure 9. **Permeant ion-dependent kinetics of SF conformational dynamics in KirBac1.1 WT and I131M. (A)** smFRET trajectories for all WT (gray) and I131M (green) traces (*n* traces given in Figs. 6 and 7) in 150 mM KCl and 150 mM NaCl were concatenated and idealized into three (low, middle, and high) FRET states (red). **(B)** Lifetime probability density function of low (L) and high (H) FRET states as a function of $[K^+]/[Na^+]$, from idealized trajectories as in A (and Figs. S3 and S4), fitted with a single exponential distribution in each case. **(C)** WT and I131M lifetimes (from fits in B) reveal qualitative dependence on ionic conditions, with H state lifetimes increasing, and L state lifetimes generally decreasing, as Na^+ is replaced by K^+. For the time constants, a monoexponential decay function was fitted to the full dataset without splitting. The time constants are represented as mean ± 95% confidence interval of the fitting.

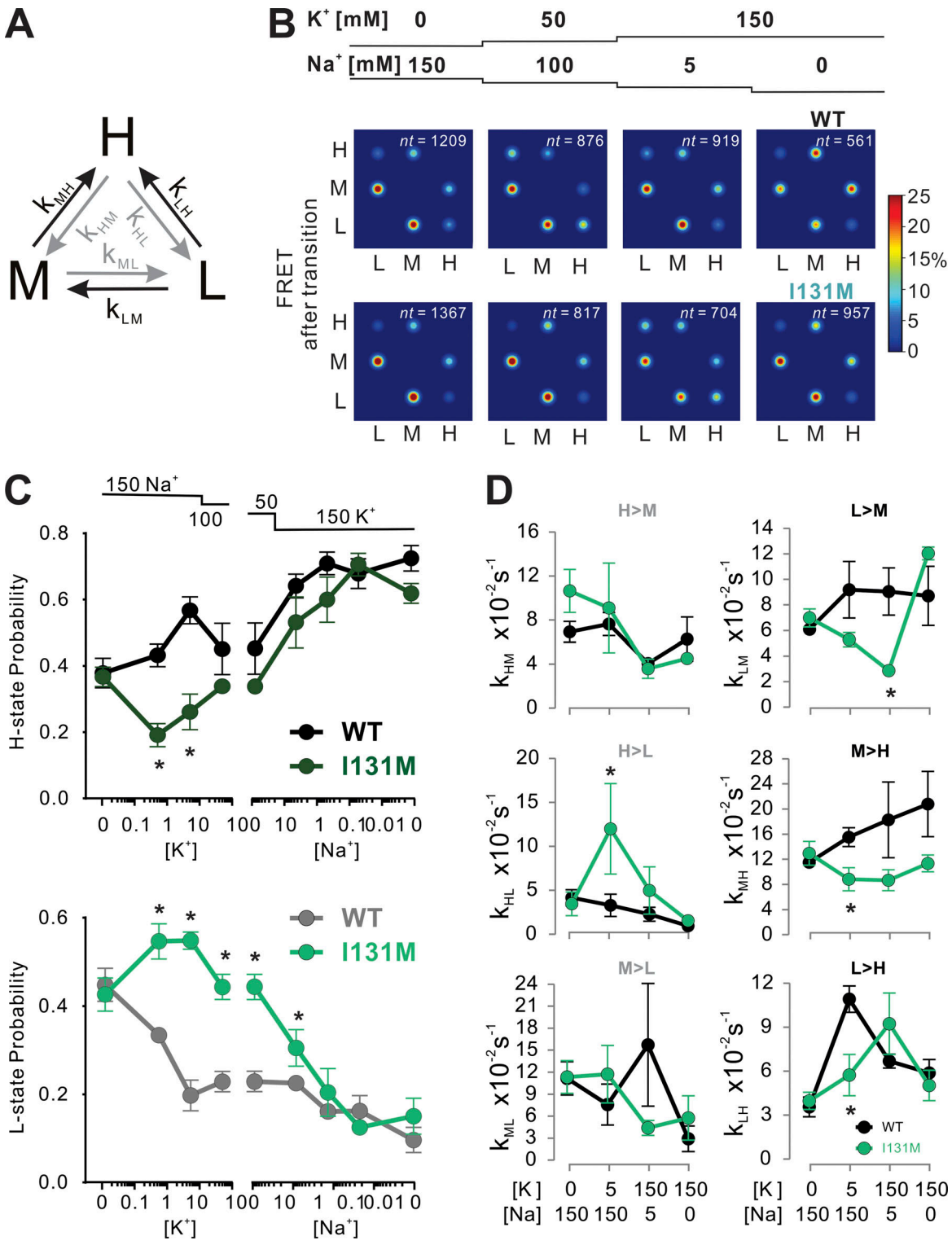

Figure 10. **Three-state ion-dependent kinetic model in KirBac1.1 WT and I131M. (A)** Three-state kinetic model for ion-dependent conformational transitions in KirBac1.1. The channels SF is presumed to exist in high FRET state (H), medium FRET state (M), and low FRET state (L). **(B)** Transition density plots (TDP) between the three states for WT and I131M in increasing [K⁺]/[Na⁺]. (*nt* indicates total number of transitions; *nt* from *n* traces given in Figs. 6 and 7). **(C)** Ion dependence of calculated state probability obtained from the idealized traces. The [K⁺]/[Na⁺] dependence of H and L state probability is weaker in I131M than in WT. **(D)** Calculated rate constants for WT and I131M as a function of [K⁺]/[Na⁺]. *, P < 0.05 versus WT. As in Fig. 8, concatenated trajectories were split into three equal-sized groups and analyzed separately to assess variability in the data, which are presented as mean ± SEM of the three data groups.

conformation represents an "induced fit," induced by K^+ ions themselves. In KirBac1.1 WT, the apparent $K_{1/2}$ for K^+-dependent conversion from the dynamic, low-FRET, nonselective conformations to the constrained, high-FRET, K-selective conformation is low (<1 mM), such that under any physiological condition, the latter conformation will predominate. However, the SF is surrounded by other structural elements, and changes in these elements could change this equilibrium, and hence change apparent selectivity.

In the present study, therefore, we examined mutations in the second transmembrane helix in KirBac1.1 (Cheng et al., 2009; Kuo et al., 2003) as models in which to probe this issue. We generated several mutants at position I131 in the TM2 domain, which is equivalent to S165 in Kir2.1 and S177 in Kir3.2. While tolerant of amino acid changes, this residue is also critical for maintenance of K^+ selectivity (Bichet et al., 2006; Bichet et al., 2004; Yi et al., 2001), but with no clear explanation of why. Our data show that the relative K^+/Na^+ selectivity is significantly reduced in mutant KirBac1.1 I131x and, in parallel, that the $[K^+]$-sensitivity of the constrained, high-FRET state and the $[K^+]$-dependence of conformational dynamics are reduced, while the Na-sensitivity of the low-FRET state is increased, in KirBac I131M. K^+-selective permeation was partially restored to I131G mutant channels specifically, by introduction of a second (F71N) mutation on the face of TM1 in contact with TM2. This suggests that appropriate structural configuration between TM1 and TM2 contributes to achieving the K-selective SF conformation (Figs. 5 and 8), as well as channel activation (Amani et al., 2020).

Implications for other channels

In demonstrating parallel shifts of ion selectivity and of the ion dependence of SF conformation, the present results provide a simple explanation for how mutation of residues that are outside the K channel SF, and which do not contact permeant ions, can nevertheless reduce ion selectivity and increase sodium permeability. As part of the structural framework around the SF, these residues control the intrinsic stability of the constrained K-selective filter conformation relative to dynamic dilated, nonselective conformations, such that mutating these residues shifts the equilibrium toward the latter. Due to the technical complexity of appropriate model systems, we have so far been unable to test the generality of this finding, and our results are so far restricted to one position in KirBac1.1 but, if replicated in other model channels, our findings will have significant implications for understanding ion selectivity in cation channel superfamily members in general. Loss of K^+ selectivity due to mutations outside the SF of multiple K channels, including KirBac1.1 [I131M], KcsA [M96V] and [E71A], or Kir3.2 [S177W] mutant channels, as well as prokaryotic K^+ selective transporters lacking the TxGYG sequence, such as TrkH and KtrB, in which only the first glycine residue in each P-loop is conserved (Cao et al., 2011; Mikušević et al., 2019; Vieira-Pires et al., 2013), raise the possibility that control of K^+ selectivity might involve more structural and environmental features (such as surrounding ions) than generally appreciated. Solid-state NMR studies have demonstrated conformational flexibility of the SF in the nonselective NaK channel (Lange et al., 2006; Bhate et al., 2010), and crystal structures of the HCN channel, which contains a GYG-containing SF yet is physiologically nonselective, reveal a considerably wider outer mouth of the pore than in K-selective K channel structures (Lee and MacKinnon, 2017). It is mere speculation, but perhaps even HCN channel SFs could adopt a K-selective conformation but are precluded from doing so by structural differences in SF-supporting elements that act to shift the $[K^+]$ dependence beyond the physiological range.

Acknowledgments

Crina M. Nimigean served as editor.

We thank Drs. Joshua Brettman, Shizhen Wang, Grigory Maksaev, and Sun-Joo Lee for helpful discussions and methodological assistance.

This work was funded by National Institutes of Health grant R35 HL140024 (to C.G. Nichols) and by a postdoctoral fellowship from the McDonnell Center for Cellular and Molecular Neurobiology, Washington University in St. Louis (to M. Matamoros).

The authors declare no competing financial interests.

Author contributions: M. Matamoros and C.G. Nichols conceived and designed the studies; M. Matamoros performed research and, with help from C.G. Nichols, analyzed data. M. Matamoros and C.G. Nichols prepared the manuscript.

Submitted: 18 June 2020
Revised: 23 November 2020
Accepted: 9 March 2021

References

Aitken, C.E., R.A. Marshall, and J.D. Puglisi. 2008. An oxygen scavenging system for improvement of dye stability in single-molecule fluorescence experiments. *Biophys. J.* 94:1826–1835. https://doi.org/10.1529/biophysj.107.117689

Alam, A., and Y. Jiang. 2011. Structural studies of ion selectivity in tetrameric cation channels. *J. Gen. Physiol.* 137:397–403. https://doi.org/10.1085/jgp.201010546

Amani, R., C.G. Borcik, N.H. Khan, D.B. Versteeg, M. Yekefallah, H.Q. Do, H.R. Coats, and B.J. Wylie. 2020. Conformational changes upon gating of KirBac1.1 into an open-activated state revealed by solid-state NMR and functional assays. *Proc. Natl. Acad. Sci. USA.* 117:2938–2947. https://doi.org/10.1073/pnas.1915010117

Andersen, O.S. 2011. Perspectives on: Ion selectivity. *J. Gen. Physiol.* 137:393–395. https://doi.org/10.1085/jgp.201110651

Bhate, M.P., B.J. Wylie, L. Tian, and A.E. McDermott. 2010. Conformational dynamics in the selectivity filter of KcsA in response to potassium ion concentration. *J. Mol. Biol.* 401:155–166. https://doi.org/10.1016/j.jmb.2010.06.031

Bichet, D., M. Grabe, Y.N. Jan, and L.Y. Jan. 2006. Electrostatic interactions in the channel cavity as an important determinant of potassium channel selectivity. *Proc. Natl. Acad. Sci. USA.* 103:14355–14360. https://doi.org/10.1073/pnas.0606660103

Bichet, D., Y.-F. Lin, C.A. Ibarra, C.S. Huang, B.A. Yi, Y.N. Jan, and L.Y. Jan. 2004. Evolving potassium channels by means of yeast selection reveals structural elements important for selectivity. *Proc. Natl. Acad. Sci. USA.* 101:4441–4446. https://doi.org/10.1073/pnas.0401195101

Blanco, M., and N.G. Walter. 2010. Analysis of complex single-molecule FRET time trajectories. *Methods Enzymol.* 472:153–178. https://doi.org/10.1016/S0076-6879(10)72011-5

Bondar, A.N., J. Baudry, S. Suhai, S. Fischer, and J.C. Smith. 2008. Key role of active-site water molecules in bacteriorhodopsin proton-transfer reactions. *J. Phys. Chem. B.* 112:14729–14741. https://doi.org/10.1021/jp801916f

Cao, Y., X. Jin, H. Huang, M.G. Derebe, E.J. Levin, V. Kabaleeswaran, Y. Pan, M. Punta, J. Love, J. Weng, et al. 2011. Crystal structure of a potassium ion transporter, TrkH. *Nature.* 471:336–340. https://doi.org/10.1038/nature09731

Cao, Y., S. Mager, and H.A. Lester. 1997. H^+ permeation and pH regulation at a mammalian serotonin transporter. *J. Neurosci.* 17:2257–2266. https://doi.org/10.1523/JNEUROSCI.17-07-02257.1997

Cheng, W.W., D. Enkvetchakul, and C.G. Nichols. 2009. KirBac1.1: It's an inward rectifying potassium channel. *J. Gen. Physiol.* 133:295–305. https://doi.org/10.1085/jgp.200810125

Cheng, W.W.L., J.G. McCoy, A.N. Thompson, C.G. Nichols, and C.M. Nimigean. 2011. Mechanism for selectivity-inactivation coupling in KcsA potassium channels. *Proc. Natl. Acad. Sci. USA.* 108:5272–5277. https://doi.org/10.1073/pnas.1014186108

Cordero-Morales, J.F., V. Jogini, A. Lewis, V. Vásquez, D.M. Cortes, B. Roux, and E. Perozo. 2007. Molecular driving forces determining potassium channel slow inactivation. *Nat. Struct. Mol. Biol.* 14:1062–1069. https://doi.org/10.1038/nsmb1309

Cuello, L.G., V. Jogini, D.M. Cortes, and E. Perozo. 2010. Structural mechanism of C-type inactivation in K^+ channels. *Nature.* 466:203–208. https://doi.org/10.1038/nature09153

Dave, R., D.S. Terry, J.B. Munro, and S.C. Blanchard. 2009. Mitigating unwanted photophysical processes for improved single-molecule fluorescence imaging. *Biophys. J.* 96:2371–2381. https://doi.org/10.1016/j.bpj.2008.11.061

Dibb, K.M., T. Rose, S.Y. Makary, T.W. Claydon, D. Enkvetchakul, R. Leach, C.G. Nichols, and M.R. Boyett. 2003. Molecular basis of ion selectivity, block, and rectification of the inward rectifier Kir3.1/Kir3.4 K^+ channel. *J. Biol. Chem.* 278:49537–49548. https://doi.org/10.1074/jbc.M307723200

Dixit, P.D., and D. Asthagiri. 2011. Thermodynamics of ion selectivity in the KcsA K^+ channel. *J. Gen. Physiol.* 137:427–433. https://doi.org/10.1085/jgp.201010533

Doyle, D.A., J. Morais Cabral, R.A. Pfuetzner, A. Kuo, J.M. Gulbis, S.L. Cohen, B.T. Chait, and R. MacKinnon. 1998. The structure of the potassium channel: molecular basis of K^+ conduction and selectivity. *Science.* 280:69–77. https://doi.org/10.1126/science.280.5360.69

Enkvetchakul, D., J. Bhattacharyya, I. Jeliazkova, D.K. Groesbeck, C.A. Cukras, and C.G. Nichols. 2004. Functional characterization of a prokaryotic Kir channel. *J. Biol. Chem.* 279:47076–47080. https://doi.org/10.1074/jbc.C400417200

Fan, J.S., and P. Palade. 1998. Perforated patch recording with beta-escin. *Pflugers Arch.* 436:1021–1023. https://doi.org/10.1007/PL00008086

Heginbotham, L., Z. Lu, T. Abramson, and R. MacKinnon. 1994. Mutations in the K^+ channel signature sequence. *Biophys. J.* 66:1061–1067. https://doi.org/10.1016/S0006-3495(94)80887-2

Hofacker, I., and K. Schulten. 1998. Oxygen and proton pathways in cytochrome c oxidase. *Proteins.* 30:100–107. https://doi.org/10.1002/(SICI)1097-0134(199801)30:1<100::AID-PROT9>3.0.CO;2-S

Joo, C., and T. Ha. 2012a. Preparing sample chambers for single-molecule FRET. *Cold Spring Harb. Protoc.* 2012:1104–1108.

Joo, C., and T. Ha. 2012b. Single-molecule FRET with total internal reflection microscopy. *Cold Spring Harb. Protoc.* 2012:pdb.top072058. https://doi.org/10.1101/pdb.top072058

Kuo, A., J.M. Gulbis, J.F. Antcliff, T. Rahman, E.D. Lowe, J. Zimmer, J. Cuthbertson, F.M. Ashcroft, T. Ezaki, and D.A. Doyle. 2003. Crystal structure of the potassium channel KirBac1.1 in the closed state. *Science.* 300:1922–1926. https://doi.org/10.1126/science.1085028

Lange, A., K. Giller, S. Hornig, M.F. Martin-Eauclaire, O. Pongs, S. Becker, and M. Baldus. 2006. Toxin-induced conformational changes in a potassium channel revealed by solid-state NMR. *Nature.* 440:959–962. https://doi.org/10.1038/nature04649

Lee, C.H., and R. MacKinnon. 2017. Structures of the human HCN1 hyperpolarization-activated channel. *Cell.* 168:111–120.e11. https://doi.org/10.1016/j.cell.2016.12.023

Liu, S., and S.W. Lockless. 2013. Equilibrium selectivity alone does not create K^+-selective ion conduction in K^+ channels. *Nat. Commun.* 4:2746. https://doi.org/10.1038/ncomms3746

Lockless, S.W., M. Zhou, and R. MacKinnon. 2007. Structural and thermodynamic properties of selective ion binding in a K^+ channel. *PLoS Biol.* 5.e121. https://doi.org/10.1371/journal.pbio.0050121

McKinney, S.A., C. Joo, and T. Ha. 2006. Analysis of single-molecule FRET trajectories using hidden Markov modeling. *Biophys. J.* 91:1941–1951. https://doi.org/10.1529/biophysj.106.082487

Mikušević, V., M. Schrecker, N. Kolesova, M. Patiño-Ruiz, K. Fendler, and I. Hänelt. 2019. A channel profile report of the unusual K^+ channel KtrB. *J. Gen. Physiol.* 151:1357–1368. https://doi.org/10.1085/jgp.201912384

Namslauer, A., H. Lepp, M. Brändén, A. Jasaitis, M.I. Verkhovsky, and P. Brzezinski. 2007. Plasticity of proton pathway structure and water coordination in cytochrome c oxidase. *J. Biol. Chem.* 282:15148–15158. https://doi.org/10.1074/jbc.M700348200

Nimigean, C.M., and T.W. Allen. 2011. Origins of ion selectivity in potassium channels from the perspective of channel block. *J. Gen. Physiol.* 137:405–413. https://doi.org/10.1085/jgp.201010551

Noskov, S.Y., and B. Roux. 2006. Ion selectivity in potassium channels. *Biophys. Chem.* 124:279–291. https://doi.org/10.1016/j.bpc.2006.05.033

Noskov, S.Y., S. Bernèche, and B. Roux. 2004. Control of ion selectivity in potassium channels by electrostatic and dynamic properties of carbonyl ligands. *Nature.* 431:830–834. https://doi.org/10.1038/nature02943

Renart, M.L., E. Montoya, A.M. Fernández, M.L. Molina, J.A. Poveda, J.A. Encinar, J.L. Ayala, A.V. Ferrer-Montiel, J. Gómez, A. Morales, and J.M. González Ros. 2012. Contribution of ion binding affinity to ion selectivity and permeation in KcsA, a model potassium channel. *Biochemistry.* 51:3891–3900. https://doi.org/10.1021/bi201497n

Rossi, M., A. Tkatchenko, S.B. Rempe, and S. Varma. 2013. Role of methyl-induced polarization in ion binding. *Proc. Natl. Acad. Sci. USA.* 110:12978–12983. https://doi.org/10.1073/pnas.1302757110

Roux, B. 2005. Ion conduction and selectivity in K^+ channels. *Annu. Rev. Biophys. Biomol. Struct.* 34:153–171. https://doi.org/10.1146/annurev.biophys.34.040204.144655

Roux, B. 2017. Ion channels and ion selectivity. *Essays Biochem.* 61:201–209. https://doi.org/10.1042/EBC20160074

Roux, B., S. Bernèche, B. Egwolf, B. Lev, S.Y. Noskov, C.N. Rowley, and H. Yu. 2011. Ion selectivity in channels and transporters. *J. Gen. Physiol.* 137:415–426. https://doi.org/10.1085/jgp.201010577

Roy, R., S. Hohng, and T. Ha. 2008. A practical guide to single-molecule FRET. *Nat. Methods.* 5:507–516. https://doi.org/10.1038/nmeth.1208

Sauer, D.B., W. Zeng, S. Raghunathan, and Y. Jiang. 2011. Protein interactions central to stabilizing the K+ channel selectivity filter in a four-sited configuration for selective K^+ permeation. *Proc. Natl. Acad. Sci. USA.* 108:16634–16639. https://doi.org/10.1073/pnas.1111688108

Shi, N., S. Ye, A. Alam, L. Chen, and Y. Jiang. 2006. Atomic structure of a Na^+- and K^+-conducting channel. *Nature.* 440:570–574. https://doi.org/10.1038/nature04508

Starace, D.M., and F. Bezanilla. 2001. Histidine scanning mutagenesis of basic residues of the S4 segment of the *Shaker* K^+ channel. *J. Gen. Physiol.* 117:469–490. https://doi.org/10.1085/jgp.117.5.469

Starace, D.M., and F. Bezanilla. 2004. A proton pore in a potassium channel voltage sensor reveals a focused electric field. *Nature.* 427:548–553. https://doi.org/10.1038/nature02270

Starace, D.M., E. Stefani, and F. Bezanilla. 1997. Voltage-dependent proton transport by the voltage sensor of the Shaker K^+ channel. *Neuron.* 19:1319–1327. https://doi.org/10.1016/S0896-6273(00)80422-5

Thompson, A.N., I. Kim, T.D. Panosian, T.M. Iverson, T.W. Allen, and C.M. Nimigean. 2009. Mechanism of potassium-channel selectivity revealed by Na^+ and Li^+ binding sites within the KcsA pore. *Nat. Struct. Mol. Biol.* 16:1317–1324. https://doi.org/10.1038/nsmb.1703

Thompson, J., and T. Begenisich. 2001. Affinity and location of an internal K^+ ion binding site in shaker K channels. *J. Gen. Physiol.* 117:373–384. https://doi.org/10.1085/jgp.117.5.373

Valiyaveetil, F.I., M. Leonetti, T.W. Muir, and R. Mackinnon. 2006. Ion selectivity in a semisynthetic K^+ channel locked in the conductive conformation. *Science.* 314:1004–1007. https://doi.org/10.1126/science.1133415

Vieira-Pires, R.S., A. Szollosi, and J.H. Morais-Cabral. 2013. The structure of the KtrAB potassium transporter. *Nature.* 496:323–328. https://doi.org/10.1038/nature12055

Wang, S., Y. Alimi, A. Tong, C.G. Nichols, and D. Enkvetchakul. 2009. Differential roles of blocking ions in KirBac1.1 tetramer stability. *J. Biol. Chem.* 284:2854–2860. https://doi.org/10.1074/jbc.M807474200

Wang, S., J.B. Brettmann, and C.G. Nichols. 2018. Studying Structural Dynamics of Potassium Channels by Single-Molecule FRET. *Methods Mol. Biol.* 1684:163–180. https://doi.org/10.1007/978-1-4939-7362-0_13

Wang, S., S.J. Lee, G. Maksaev, X. Fang, C. Zuo, and C.G. Nichols. 2019. Potassium channel selectivity filter dynamics revealed by single-molecule FRET. *Nat. Chem. Biol.* 15:377–383. https://doi.org/10.1038/s41589-019-0240-7

Wang, S., R. Vafabakhsh, W.F. Borschel, T. Ha, and C.G. Nichols. 2016. Structural dynamics of potassium-channel gating revealed by single-molecule FRET. *Nat. Struct. Mol. Biol.* 23:31–36. https://doi.org/10.1038/nsmb.3138

Wikström, M. 1998. Proton translocation by bacteriorhodopsin and heme-copper oxidases. *Curr. Opin. Struct. Biol.* 8:480–488. https://doi.org/10.1016/S0959-440X(98)80127-9

Yang, J., M. Yu, Y.N. Jan, and L.Y. Jan. 1997. Stabilization of ion selectivity filter by pore loop ion pairs in an inwardly rectifying potassium channel. *Proc. Natl. Acad. Sci. USA.* 94:1568–1572. https://doi.org/10.1073/pnas.94.4.1568

Yi, B.A., Y.F. Lin, Y.N. Jan, and L.Y. Jan. 2001. Yeast screen for constitutively active mutant G protein-activated potassium channels. *Neuron.* 29:657–667. https://doi.org/10.1016/S0896-6273(01)00241-0

Zhou, Y., J.H. Morais-Cabral, A. Kaufman, and R. MacKinnon. 2001. Chemistry of ion coordination and hydration revealed by a K^+ channel-Fab complex at 2.0 A resolution. *Nature.* 414:43–48. https://doi.org/10.1038/35102009

Supplemental material

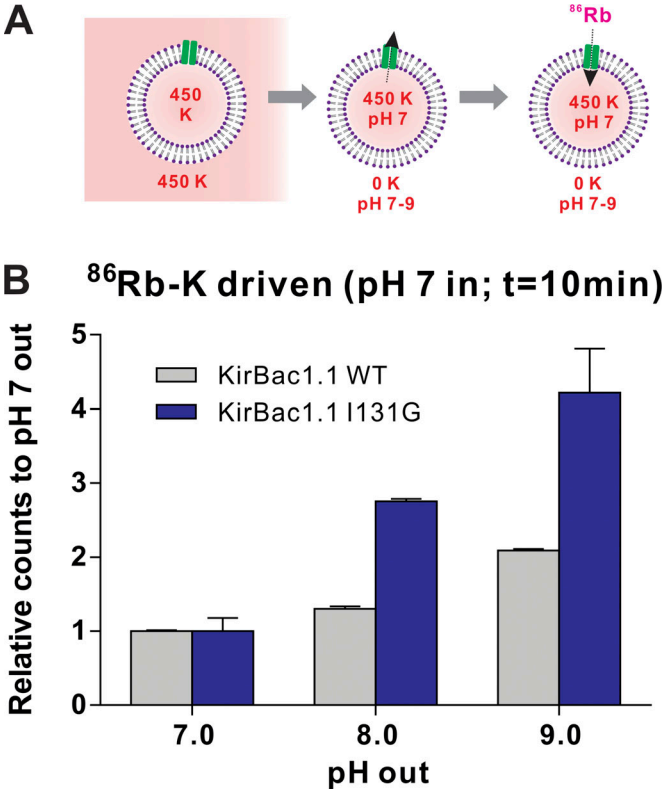

Figure S1. **The I131G mutant is more permeable to protons. (A)** Schematic diagram of K-driven $^{86}Rb^{+}$ assays with external pH values varying from 7 to 9. **(B)** Relative counts of $^{86}Rb^{+}$ uptake after 10 min for KirBac1.1 WT (gray bars) and KirBac1.1 I131G (blue bars) with increasing pH (7–9), normalized to counts at pH 7. All data are represented as mean ± SEM of at least n = 3 experiments.

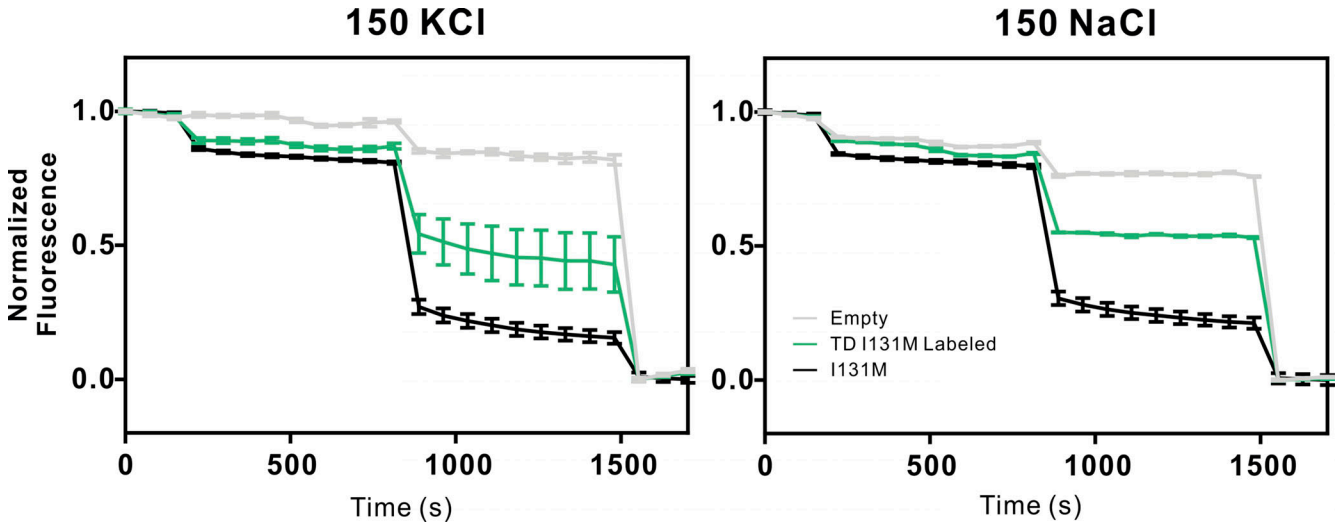

Figure S2. **The I131M-labeled tandem dimer retains functionality.** As for the WT-labeled tandem dimer (Wang et al., 2016, 2019), the I131M-labeled tandem dimer in position T120C is functional in Na^+ and K^+. All data are represented as mean ± SEM of at least n = 3 experiments.

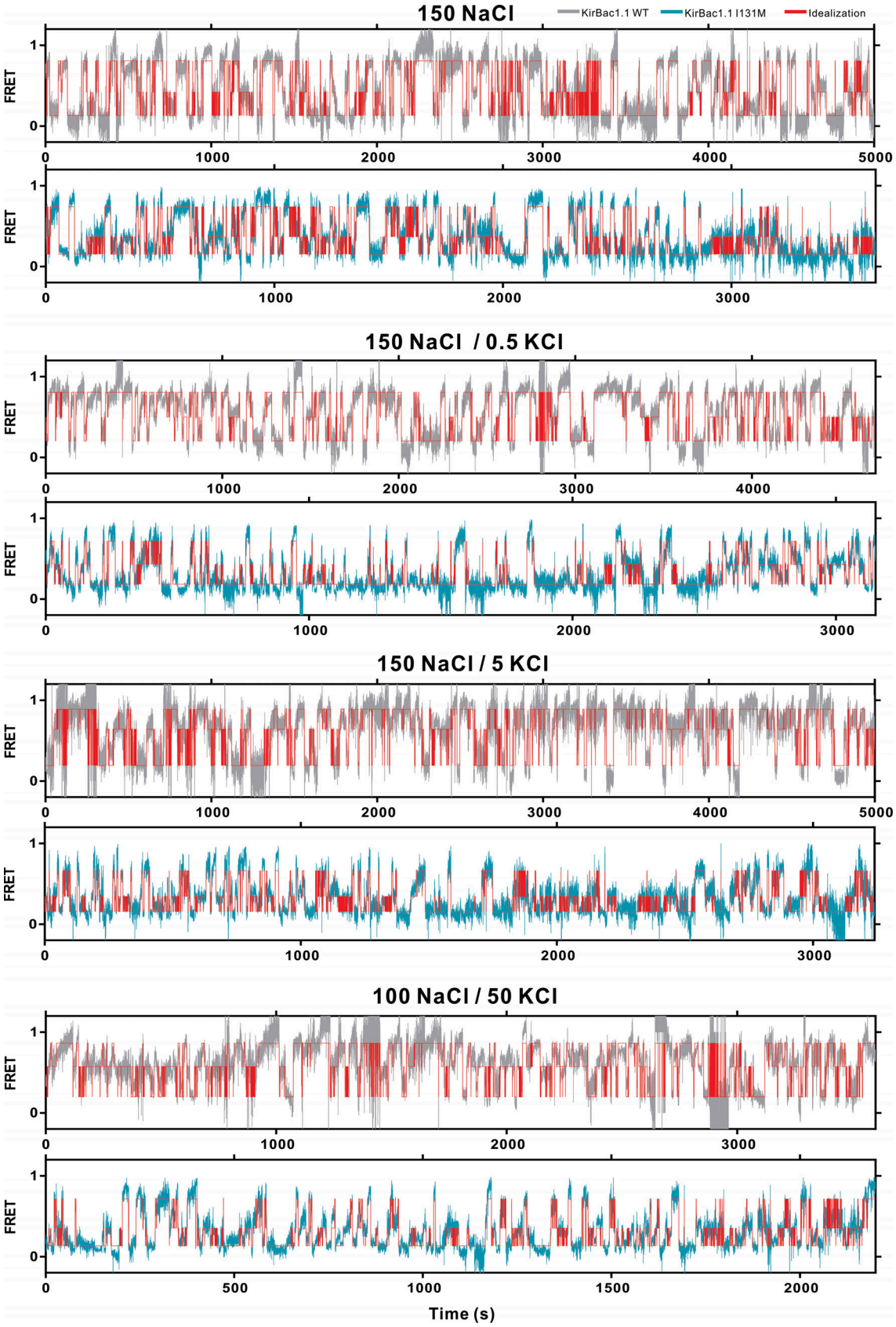

Figure S3. **Low K⁺–dependent kinetics of SF in KirBac1.1 WT and I131M.** Concatenated smFRET trajectories of WT (gray) and I131M (green) in 150 mM NaCl with zero K⁺, 0.5 mM K⁺, 5 mM K⁺, and 100 mM Na⁺ + 50 mM K⁺, as indicated, together with three state idealizations (red) corresponding to low, middle, and high FRET states.

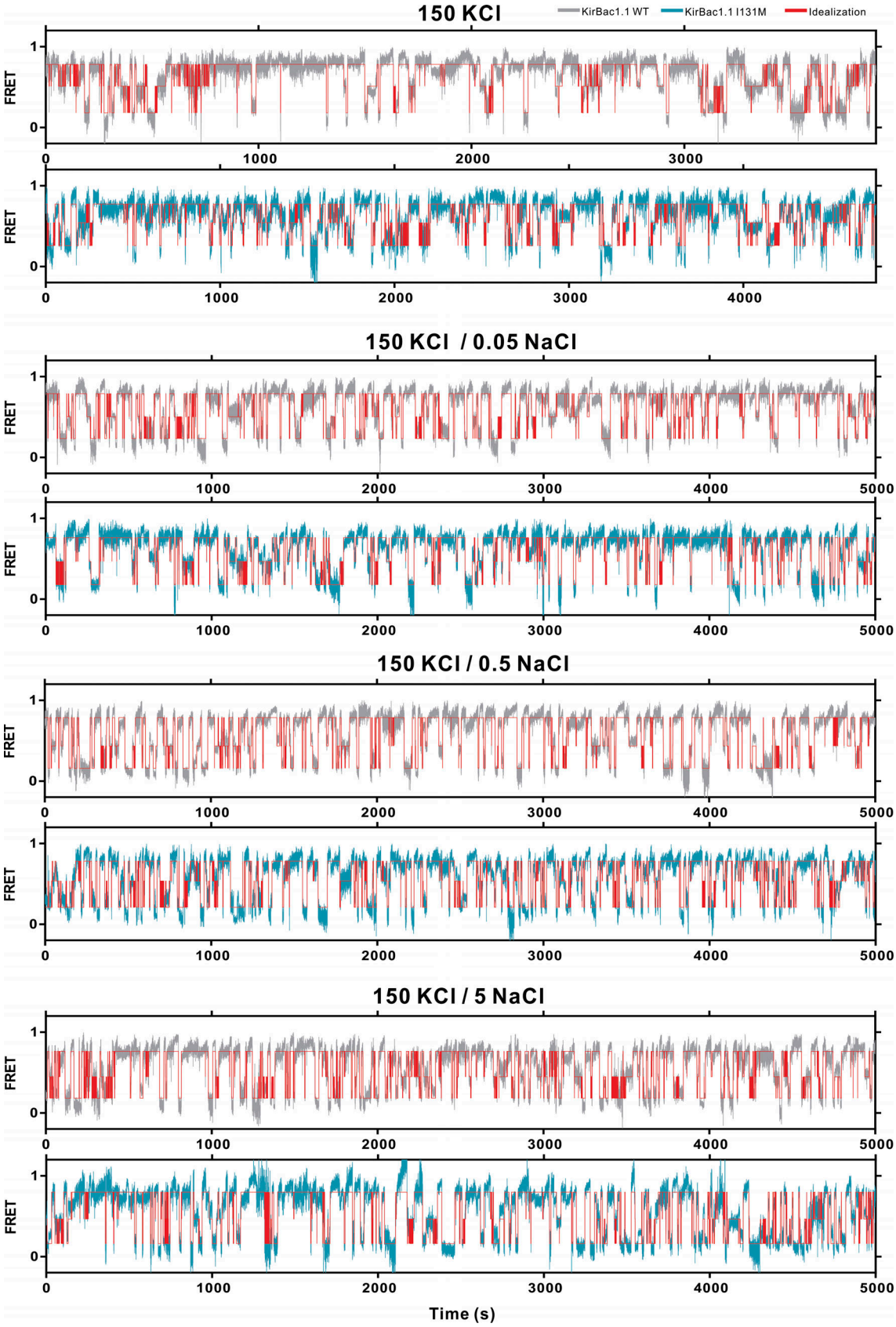

Figure S4. **Low Na^+–dependent kinetics of SF in KirBac1.1 WT and I131M.** Concatenated smFRET trajectories of WT (gray) and I131M (green) in 150 mM KCl with zero Na^+, 0.05 mM Na^+, 0.5 mM Na^+, or 5 mM Na^+, as indicated, together with three state idealizations (red) corresponding to low, middle, and high FRET states.

Provided online are two tables. Table S1 lists the number of individual molecules and identified transitions for idealized smFRET records. Table S2 lists individual rate constants for the three-state model.